

# Noninvasive and Point-of-Care Surface-Enhanced Raman Scattering (SERS)-Based Breathalyzer for Mass Screening of Coronavirus Disease 2019 (COVID-19) under 5 min

Shi Xuan Leong,<sup>¶</sup> Yong Xiang Leong,<sup>¶</sup> Emily Xi Tan, Howard Yi Fan Sim, Charlynn Sher Lin Koh, Yih Hong Lee, Carice Chong, Li Shiuan Ng, Jaslyn Ru Ting Chen, Desmond Wei Cheng Pang, Lam Bang Thanh Nguyen, Siew Kheng Boong, Xuemei Han, Ya-Chuan Kao, Yi Heng Chua, Gia Chuong Phan-Quang, In Yee Phang, Hiang Kwee Lee, Mohammad Yazid Abdad, Nguan Soon Tan, and Xing Yi Ling\*



Cite This: <https://doi.org/10.1021/acsnano.1c09371>



Read Online

ACCESS |



Metrics & More



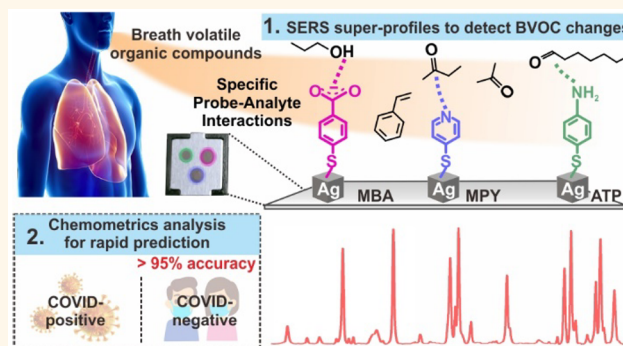
Article Recommendations



Supporting Information

**ABSTRACT:** Population-wide surveillance of COVID-19 requires tests to be quick and accurate to minimize community transmissions. The detection of breath volatile organic compounds presents a promising option for COVID-19 surveillance but is currently limited by bulky instrumentation and inflexible analysis protocol. Here, we design a hand-held surface-enhanced Raman scattering-based breathalyzer to identify COVID-19 infected individuals in under 5 min, achieving >95% sensitivity and specificity across 501 participants regardless of their displayed symptoms. Our SERS-based breathalyzer harnesses key variations in vibrational fingerprints arising from interactions between breath metabolites and multiple molecular receptors to establish a robust partial least-squares discriminant analysis model for high throughput classifications. Crucially, spectral regions influencing classification show strong corroboration with reported potential COVID-19 breath biomarkers, both through experiment and in silico. Our strategy strives to spur the development of next-generation, noninvasive human breath diagnostic toolkits tailored for mass screening purposes.

**KEYWORDS:** surface-enhanced Raman scattering (SERS), coronavirus disease 2019 (COVID-19), breath volatile organic compounds (BVOCs), breathomics, mass screening



One of the key strategies to curb Coronavirus Disease 2019 (COVID-19) transmissions is to develop rapid and accurate mass screening tools to identify infectious yet asymptomatic individuals for isolation. These screening tools complement polymerase chain reaction (PCR) tests as they play a critical role in filtering out most healthy individuals from the general population and avoid overloading of PCR testing facilities which can otherwise retard pandemic response. An emerging solution is the noninvasive breath test, where breath volatile organic compounds (BVOCs) function as COVID-19 specific biomarkers. Notably, recent studies have

shown that the coronavirus-induced immune responses and metabolic changes can alter concentrations of BVOCs such as aldehydes, ketones, and alcohols, enabling the identification of COVID-positive individuals regardless of their symptoms.<sup>1–4</sup>

**Received:** October 22, 2021

**Accepted:** January 6, 2022



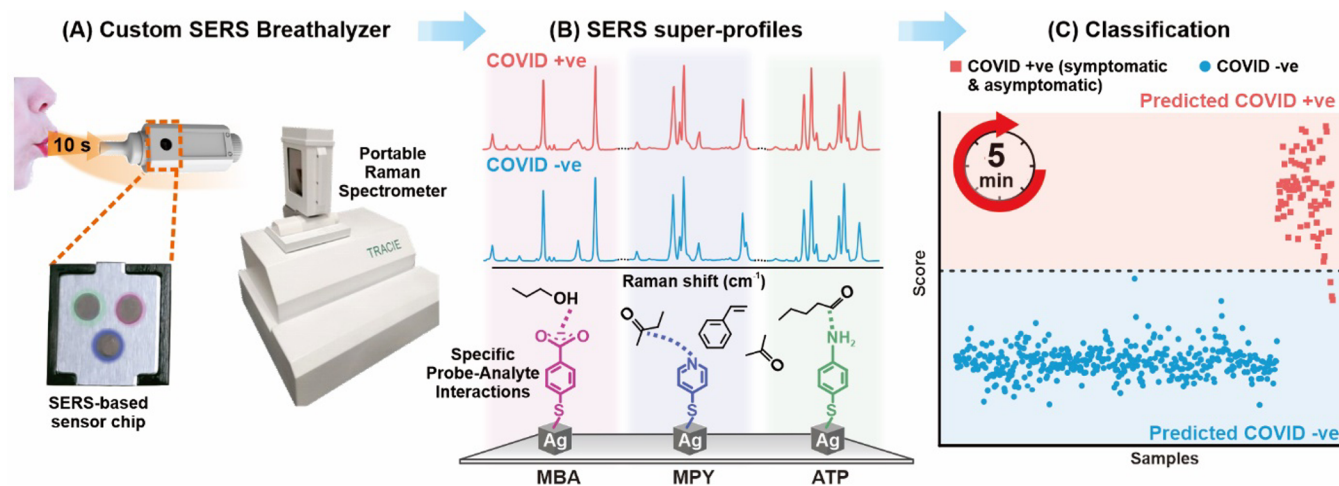


**Figure 1.** Overview of our SERS-based strategy to identify COVID-positive individuals using their breath volatile organic compounds (BVOCs).

Gas chromatography coupled mass spectrometry (GC–MS) is the current gold standard used for concurrent separation and identification of key compounds in the human breath.<sup>5–7</sup> However, these instruments are typically costly and bulky, making it less ideal to upscale and integrate as a mass screening tool for on-site deployment. In addition, the need to exhale directly into the instrument also creates a bottleneck in analysis time where multiple breath collections and subsequent analyses cannot be done in parallel. Hence, there is an urgent need to develop a simple, portable, and inexpensive mass screening tool that can analyze COVID-19 related BVOCs.

Herein, we design a surface-enhanced Raman scattering (SERS)-based breathalyzer to distinguish BVOC profiles of COVID-positive individuals, achieving >95% sensitivity and specificity across 501 participants from clinical case-control studies conducted in Singapore (Figure 1). Our breathalyzer encompasses a SERS sensor that is nested within a custom-made, hand-held, single-use breath chamber to facilitate the safe collection of breath samples, with measurements performed on-site using a portable Raman spectrometer. Participants are simply required to blow continuously into the breath chamber for 10 s and can receive their test result within 5 min, since there is no need for any sample pretreatment (Figure 1; Figure S1). Upon exposure to breath, molecular receptors with various active chemical functionalities on our SERS sensor form complementary receptor–BVOC interactions such as ion–dipole interactions or hydrogen bonding with the diverse range of BVOCs present. These interactions elicit specific spectral variations, which can be serially combined as a SERS “superprofile” to accentuate minute differences in BVOC compositions between COVID-positive and COVID-negative individuals. Scrutiny of their respective SERS superprofiles reveal key spectral regions that are consistent with experimental and *in silico* spectral changes observed when our sensor is exposed to pure VOC vapors of potential COVID-19 biomarkers. Crucially, we demonstrate that these spectral differences are independent of displayed COVID-19 symptoms and other potential confounding factors such as participants’ age, gender, smoking habits, and time since their last meal. For high throughput spectral analyses, we construct a classification model using partial least-squares discriminant analysis (PLSDA) that can be seamlessly incorporated with most Raman measurement software to provide instantaneous results. In addition, our workflow features decoupled sample collection

and measurement to allow maximum deployment flexibility in practice. Overall, our study showcases the promising potential of utilizing SERS-based sensors in the analysis and differentiation of breath metabolites among infected and noninfected people to achieve rapid and noninvasive disease detection. It signifies a decisive step forward in the practical application of SERS for next-generation, point-of-care diagnostic toolkits of other respiratory and nonrespiratory diseases, not limited to COVID-19.

## RESULTS AND DISCUSSION

**Fabrication and Characterization of Our Multireceptor SERS Sensor.** To effectively discriminate COVID-positive breath profiles, we design multiple surface receptors on our SERS sensor to induce a myriad of complementary intermolecular interactions with the BVOCs present as the breath sample flows through the breath chamber. Our sensor comprises arrays of Ag nanocubes (edge length =  $120 \pm 5$  nm, Figure S2) with 4-mercaptobenzoate (MBA), 4-mercaptopyridine (MPY), and 4-aminothiophenol (ATP) functionalized onto the nanocube surface as molecular receptors (Figure 1; Figure S3). The multireceptor SERS sensor is strategically designed to possess specific functional groups that can chemically interact with BVOCs via hydrogen bonding, ion–dipole interactions and  $\pi$ – $\pi$  interactions to bring the gaseous analytes close to the plasmonic surface.<sup>8,9</sup> Our SERS sensor exhibits a high SERS analytical enhancement factor of  $1.4 \times 10^{10}$ , owing to strong electromagnetic enhancement from the sharp Ag nanocube edges and intense inter-nanocube plasmonic coupling, which enables ultrasensitive analyte detection (Figure S4; Supporting Information 1).<sup>10</sup> In addition, an excellent signal reproducibility of <4% signal standard deviation ensures that our SERS measurements are consistent and reproducible (Figure S5). The sensors were subsequently assembled into single-use breath chambers customized with infection control safety features that ensure high safety and hygiene standards (refer to Materials and Methods). We further demonstrate the robustness of our sensor, which displays similar signal consistencies after sensor assembly and over time, with no signs of nanocube oxidation even after breath exposure (Figure S6). We also affirm that our SERS sensor can detect various VOCs at their physiologically relevant levels, as evidenced from the well-separated spectral clusters in the principal component analysis (PCA) score plot (Figure S7).

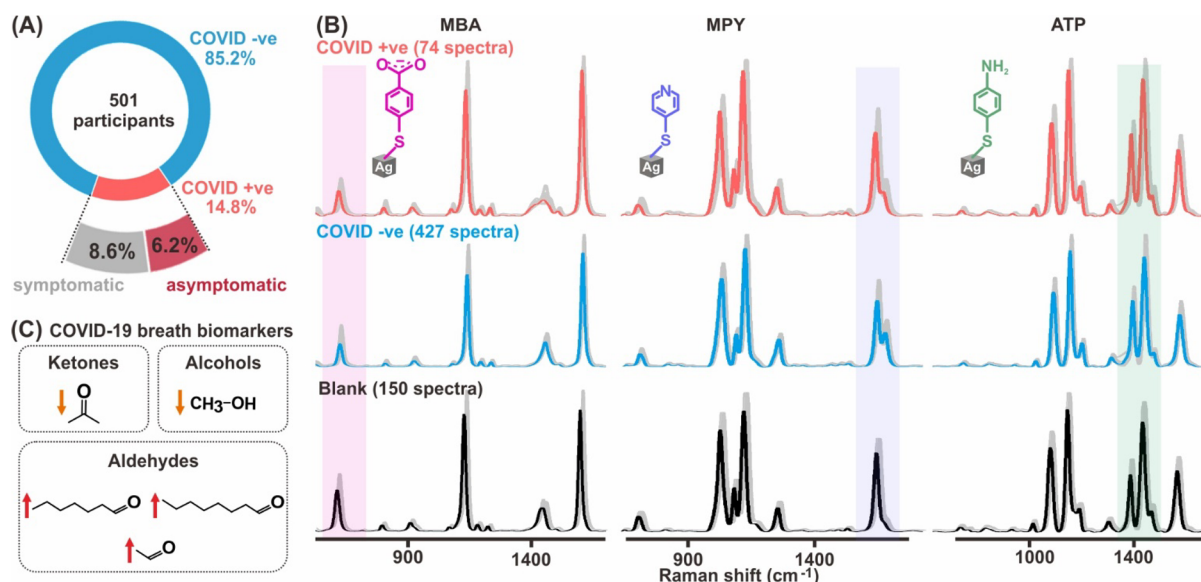


**Figure 2.** SERS profiles of breath samples acquired through case-control clinical trials. (A) Schematic summary of COVID-19 infection status and outward display of flu-like symptoms of 501 participants. (B) Representative SERS spectra of each molecular receptor (MBA, MPY, ATP) in the absence (referred to as “blank”) and presence of COVID-positive and COVID-negative breath samples. Peaks of interest with in-depth analysis are highlighted. A total of 150 blank, 74 COVID-positive, and 427 COVID-negative samples are measured. (C) Molecular structures of reported COVID-19 breath biomarkers. The relative BVOC concentration changes in COVID-positive individuals compared to changes in COVID-negative individuals are indicated by the arrows.

**SERS Spectral Investigations of COVID-Positive and COVID-Negative Individuals.** To investigate the ability of our SERS sensor in differentiating COVID-positive and COVID-negative breath profiles, we conducted a comparative case-control clinical trial in Singapore involving 501 participants. Participants were required to take a deep breath and exhale continuously into a fresh breath chamber for 10 s under supervision to collect alveolar air from deeper lung regions which are involved in lung-blood VOC exchange (Figure S1).<sup>7,11</sup> Each blown breath chamber was allowed to incubate for a minimum of 2 min to allow sufficient time for receptor–VOC interactions to occur before measuring the SERS spectra using a portable Raman spectrometer (Figure S8). The whole process takes less than 5 min, which is crucial for application in mass screenings. Subsequently, a nasopharyngeal swab specimen was collected from the participants for a PCR test within 48 h of breath collection as a benchmark to determine if they were COVID-negative or COVID-positive. Of all the participants, 74 participants (14.8%) were classified as COVID-positive on the basis of their PCR test results, with 31 being asymptomatic at the point of testing (Figure 2A).

Scrutiny of the SERS spectra in the absence of breath (denoted as “blank”, total 150 samples), presence of COVID-positive breath (total 74 samples) and presence of COVID-negative breath (total 427 samples) reveals several crucial spectral differences, which clearly distinguish the breath chemical profiles of COVID-positive and COVID-negative individuals (Figure 2B). To gain qualitative insight on key receptor–BVOC interactions behind these spectral differences, we compare the observed breath-induced spectral differences against individual SERS responses to several reported VOC biomarkers in the breaths of COVID-positive patients. The target VOCs of interest include methanol, ethanal, heptanal, octanal, and acetone (Figure 2C).<sup>1–3</sup> In addition, water vapor is included to investigate its potential influence in the resulting SERS signals. Briefly, the SERS sensor was separately incubated

with neat standards in closed systems to allow vaporization of the respective VOC into an equilibrium state (Supporting Information 2). For in-depth spectral analysis, we select three spectral regions, namely, 490–550  $\text{cm}^{-1}$  of MBA, 1560–1680  $\text{cm}^{-1}$  of MPY, and 1050–1500  $\text{cm}^{-1}$  of ATP (Figure 2B). It is important to note that all investigated differences across blanks, COVID-positive, and COVID-negative breath samples are statistically different at 95% confidence level with  $p$  values <0.05, using the Mann–Whitney rank-sum test (Materials and Methods; Table S2). This indicates that the identified features are relevant and can be utilized to differentiate COVID-positive and COVID-negative individuals.

For MBA, we observe a decrease in peak intensity of the C–S stretching ( $\nu(\text{CS})$ ) peak at 521  $\text{cm}^{-1}$ , from  $0.29 \pm 0.03$  in blanks to  $0.19 \pm 0.05$  and  $0.22 \pm 0.09$  in the presence of COVID-positive and COVID-negative breaths, respectively, with COVID-positive samples exhibiting a larger decrease than COVID-negative samples (Figure 3Aii,iii).<sup>12</sup> The  $\nu(\text{CS})$  peak intensity reflects the relative polarizability of the C–S bond and changes when carbonyl compounds such as ethanal, heptanal, octanal, and acetone form ion–dipole interactions or hydroxyl-containing compounds such as methanol and water vapor form hydrogen bonding with MBA, resulting in a redistribution of the delocalized electron cloud (Figure 3Ai).<sup>13</sup> Experimentally, a decrease in  $\nu(\text{CS})$  peak intensity is observed upon separate exposure to pure vapors of ethanal, heptanal, octanal, and acetone, while an increase is observed upon exposure to methanol and water (Figure 3Aiv, Table S3). This trend is in good qualitative agreement with simulated SERS spectra obtained using density functional theory (DFT), where ethanal, heptanal, octanal, and acetone induce a 0.23–29% decrease, while methanol and water vapor induce a 11–32% increase in  $\nu(\text{CS})$  peak intensity (Table S3). The observation of a larger decrease in  $\nu(\text{CS})$  peak intensity for COVID-positive breath profiles is therefore consistent with lower methanol and higher aldehyde (ethanal, heptanal, and octanal) levels reported in

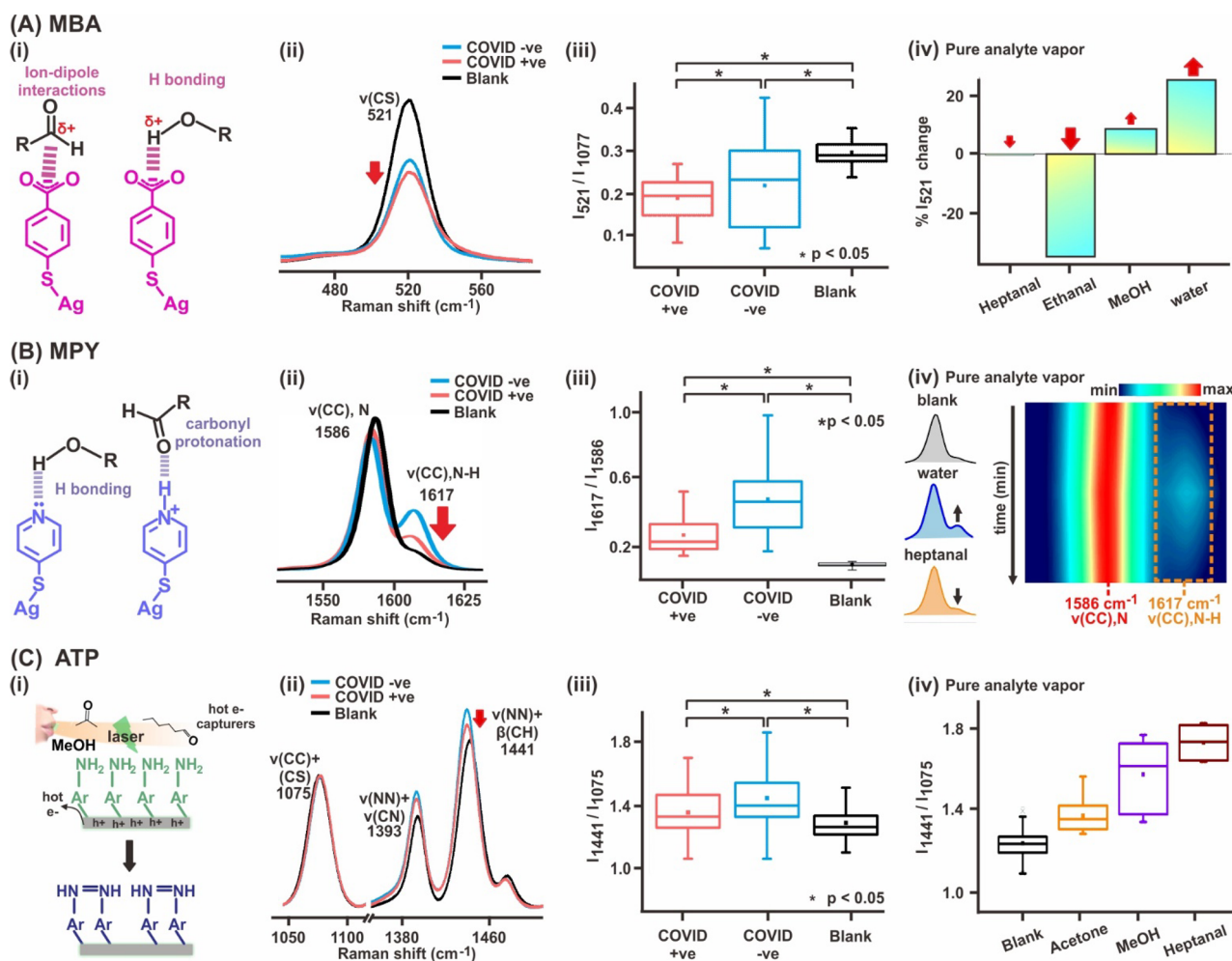


**Figure 3.** SERS analysis of breath samples of COVID-positive and COVID-negative participants. (A) (i) Illustration of ion–dipole interactions between MBA-aldehydes and H-bonding with hydroxyl-containing compounds. (ii)  $521\text{ cm}^{-1}$  SERS peak of MBA for blanks, COVID-positive, and COVID-negative breath samples. (iii) Box plots comparing the  $521\text{ cm}^{-1}$  peak intensity using the  $1077\text{ cm}^{-1}$  peak intensity as an internal standard. (iv) Bar charts describing experimental percentage change in the  $521\text{ cm}^{-1}$  peak intensity upon exposure to selected pure vapors, using the  $1077\text{ cm}^{-1}$  peak as the internal intensity standard. (B) (i) Illustration of deprotonated and protonated MPY forming hydrogen bonds with aldehydes and hydroxyl-containing compounds. (ii) MPY  $I_{1617}/I_{1586}$  SERS peak intensity ratio for blanks, COVID-positive, and COVID-negative breath samples. (iii) Box plots comparing the  $I_{1617}/I_{1586}$  peak intensity ratios. (iv) Evolution of the  $1550\text{--}1625\text{ cm}^{-1}$  region upon first exposure to water vapor, followed by heptanal vapor. Intensities are normalized to the  $1586\text{ cm}^{-1}$  peak. Schematic illustration of analyte-induced changes in peak intensity ratios are included as inset. (C) (i) Illustration of increased laser-induced ATP dimerization to DMAB in the presence of breath metabolites that serve as hot electron acceptors. (ii) ATP  $1030\text{--}1600\text{ cm}^{-1}$  SERS spectral region for blanks, COVID-positive, and COVID-negative breath samples. (iii) Box plots comparing the  $1441\text{ cm}^{-1}$  peak intensity using the  $1075\text{ cm}^{-1}$  peak intensity as an internal standard. (iv) Box plots comparing the  $1441\text{ cm}^{-1}$  peak intensity after exposure to selected pure vapors, using the  $1075\text{ cm}^{-1}$  peak intensity as an internal standard. All statistical significances, determined by the Mann–Whitney rank sum test at  $p < 0.05$  level, is indicated by \*. For all box plots, the mean and median are represented by the square box symbol and horizontal line, respectively. The main box covers the lower to upper quartiles while the whiskers are extended to cover all data points that lie within  $\pm 1.5$  interquartile range.

literature.<sup>1–3</sup> The general decrease in  $\nu(\text{CS})$  intensity for samples exposed to breath indicates a stronger influence of ion–dipole interactions in the C–S bond polarizability. As a result, the effect of relative humidity in the exhaled breath samples on the MBA  $\nu(\text{CS})$  peak intensity is minimal.

For MPY, we observe an increase in peak intensity ratio of  $1586$  and  $1617\text{ cm}^{-1}$  ( $I_{1617}/I_{1586}$ ), from  $0.091 \pm 0.011$  in blanks to  $0.265 \pm 0.116$  and  $0.477 \pm 0.194$  in the presence of COVID-positive and COVID-negative breath, respectively, with COVID-positive samples exhibiting a lower increase than COVID-negative samples (Figure 3Bii,iii). The  $1586$  and  $1617\text{ cm}^{-1}$  peak is indexed to the aromatic C=C stretching  $\nu(\text{CC})$  when the pyridine nitrogen is deprotonated and protonated, respectively; hence  $I_{1617}/I_{1586}$  describes the relative

amount of protonated pyridine species present.<sup>14</sup> Before breath exposure, MPY exists predominantly in the deprotonated state, as indicated by the low  $I_{1617}/I_{1586}$  in blank samples. After breath exposure, pseudoprotonated pyridine species are formed through hydrogen bonding between MPY and hydroxyl-containing compounds such as methanol and water vapor, resulting in an intensification of the  $1617\text{ cm}^{-1}$  peak and an increase in  $I_{1617}/I_{1586}$  (Figure 3Bi).<sup>15,16</sup> A similar increase in  $I_{1617}/I_{1586}$  is observed experimentally upon separate exposure to pure vapors of methanol and water (Figure 3Biv; Figure S9). It should be noted that exposure to carbonyl compounds such as ethanal, heptanal, octanal, and acetone after incubation with water vapor induces a slight reduction of the  $1617\text{ cm}^{-1}$  peak intensity; however, their respective  $I_{1617}/I_{1586}$  remains higher

than blank samples. The reduction is triggered by a decrease in protonated pyridine species because carbonyl compounds compete for protons to form protonated carbonyl species (Figure 3Bi, Figure S9). The observation of a smaller increase in  $I_{1617}/I_{1586}$  for COVID-positive breath profiles is therefore well-aligned with lower methanol and higher aldehyde (ethanal, heptanal, and octanal) levels reported in literature.<sup>1–3</sup>

For ATP, the azobenzene N=N stretching coupled with C–H bending ( $\nu(\text{NN}) + \beta(\text{CH})$ ) at  $1441\text{ cm}^{-1}$  intensifies from  $1.272 \pm 0.116$  in blanks to  $1.339 \pm 0.179$  and  $1.430 \pm 0.187$  in the presence of COVID-positive and COVID-negative breath, respectively, with COVID-positive samples registering a smaller increase than COVID-negative samples (Figure 3Cii,iii). The  $\nu(\text{NN}) + \beta(\text{CH})$  is a vibrational mode characteristic of *p,p'*-dimercaptoazobenzene (DMAB) formed by laser-induced dimerization of ATP.<sup>17</sup> The observed intensification of the  $\nu(\text{NN}) + \beta(\text{CH})$  peak can be attributed to increased and faster ATP dimerization facilitated by VOCs present in breath, which capture hot electrons generated by surface plasmon decay, increasing the number of hot holes available to form DMAB (Figure 3Ci).<sup>18–20</sup> This explains similar intensity trends observed for other characteristic DMAB peaks at 1143, 1186, and  $1393\text{ cm}^{-1}$  (Figure S10). With separate exposure to pure vapors of ethanal, heptanal, octanal, acetone, methanol, and water, we observe a similar increase in DMAB-associated peak intensities at 1143 and  $1441\text{ cm}^{-1}$  (Figure 3Civ; Figure S10). The observation of a smaller increase in the  $\nu(\text{NN}) + \beta(\text{CH})$  peak intensity for COVID-positive breath profiles is therefore in good agreement with lower methanol and acetone levels reported in the literature.<sup>1–3</sup> Notably, the combined effect of lower methanol and acetone levels is more pronounced than elevated aldehyde (ethanal, heptanal, octanal) levels, suggesting that the cumulative effect on ATP is likely to be dominated by the former. It is important to note that in addition to the aforementioned peaks, we also observe other spectral differences including MBA's ring breathing + C–S stretching ( $1077\text{ cm}^{-1}$ ), MPY's ring breathing ( $1014\text{ cm}^{-1}$ ) and C–H + N–H bending ( $1224\text{ cm}^{-1}$ ), and ATP's DMAB-associated peaks ( $1143$ ,  $1186$ , and  $1393\text{ cm}^{-1}$ ), which facilitate differentiation (Figures S11–S13).

By establishing a strong correlation between observed receptor spectral variances upon exposure to COVID-positive and COVID-negative breath samples, as well as with pure vapors of reported COVID-19 biomarkers, we affirm that our SERS sensor effectively captures the distinct breath profile of a COVID-positive individual. The nonspecific nature of our SERS sensor effectively records the cumulative response of each receptor to all BVOCs present, with each receptor exhibiting pronounced spectral differences between COVID-positive and COVID-negative individuals. When the different SERS responses of individual receptors are combined, these spectral changes can reinforce one another to form characteristic SERS “breath-prints” that can be used as specialized identifiers of an individual's COVID-19 infection status. Such a recognition technique is highly advantageous because it eliminates the need to isolate and identify individual components for class differentiation, which is tedious and cumbersome.

**Rapid COVID-19 Classification Using Partial Least-Squares Discriminant Analysis.** With an in-depth understanding of the spectral regions contributing to the differentiation of breath profiles based on their COVID-19 infection status, we construct a binary classification model using partial least-squares discriminant analysis (PLSDA) to achieve rapid,

high throughput analyses. PLSDA is an established technique that maximizes and combines the largest SERS spectral covariances between different data sets as latent variables (LVs) to achieve maximum differentiation between COVID-19-positive and COVID-19-negative breath profiles.<sup>21–23</sup> In addition, the algorithm requires minimal computational power and produces classification scores that are easily comprehensible, making it particularly suitable for our application as a mass screening tool. Before the PLSDA model is constructed, SERS spectra derived from all three receptors are baseline corrected, normalized, and concatenated as a single SERS superprofile (Figure 4D). Each SERS superprofile effectively harnesses spectral variances arising from receptor–BVOC interactions, creating an additive effect that enhances the differentiation of

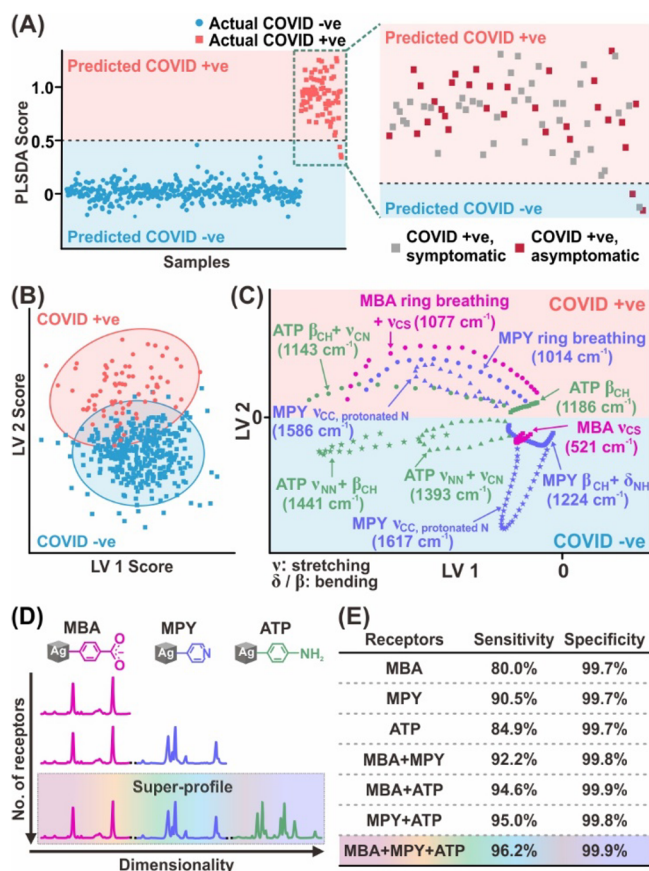


**Figure 4.** Partial least-squares discriminant analysis (PLSDA) for rapid, high throughput classification of breath profiles based on their COVID-19 infection status. (A) PLSDA score plot derived from the classification of individual SERS superprofiles showing clear distinction between the breath profiles of COVID-positive and COVID-negative individuals. Inset shows the zoomed-in segment of the PLSDA score plot for COVID-positive individuals, illustrating that symptoms do not affect their classification scores. (B) PLSDA score plot of the first two latent variables (LVs), highlighting the influence of LV 2 in classifying COVID-positive and COVID-negative individuals. (C) PLSDA loadings plot for the first two LVs to illustrate specific receptor vibrational modes which influence the classification of COVID-positive and COVID-negative individuals. (D) Scheme depicting the formation of SERS superprofiles using spectral information from multiple receptors to increase the data dimensionality. (E) Summary table comparing the classification sensitivity and specificity for an increasing number of receptors using averaged classification outcomes across 50 model iterations.

COVID-positive and COVID-negative classes. Next, a random stratified sampling algorithm is used to split the data set into a train set and prediction set comprising 80% and 20% of the original data set, respectively, over 50 different iterations to generate 50 classification outcomes with each prediction set. Such iterations minimize any potential issues with selection bias, chance classification outcomes, and model overfit.<sup>24,25</sup>

Overall, the PLSDA model achieves an average classification sensitivity of 96.2% and specificity of 99.9% when distinguishing COVID-positive and COVID-negative breath profiles (Figure 4A, Table S4, Supporting Information 3). Using triplicate breaths, we affirm that our PLSDA model classification is reproducible and consistent (Figure S14). The low average false-negative rate of 3.8% is superior to commercially available antigen rapid tests with reported false-negative rates of 10–30% and is comparable to PCR tests given similar sample sizes.<sup>26–28</sup> Notably, asymptomatic COVID-positive individuals can be accurately classified, indicating that characteristic BVOC changes do occur and can be detected regardless of symptoms (Figure 4A inset). This is consistent with recent studies reporting that the lack of symptoms does not preclude internal physiological changes.<sup>29,30</sup> Timely detection of such asymptomatic individuals through active mass screening is especially critical to disrupt the silent viral spread into local communities that often remains undetected until a massive outbreak occurs.

We further use the PLSDA score and loadings plot to highlight how different receptor spectral regions influence the classification outcome, so as to establish a robust relationship between the classification results and previously identified regions which showed distinct differences (Figure 4B,C). The first two LVs of are important in describing regions that contribute to the largest variances between the two classes.<sup>31,32</sup> From the score plot, we observe that COVID-positive breath samples typically show more positive LV 2 scores while COVID-negative breath samples show more negative LV 2 scores (Figure 4B). We note that the distribution of data points along LV 1 for both class groups is due to intraclass variances, which can be attributed to variations in BVOC concentrations among different individuals.<sup>33</sup> Nonetheless, this does not affect the COVID-positive/negative clustering along LV 2. In combination with the loadings plot, we can then correlate spectral regions which are assigned positive LV 2 scores as regions contributing more significantly to a COVID-positive classification outcome, and vice versa (Figure 4C). For instance, MBA's C–S stretching ( $1077\text{ cm}^{-1}$ ), MPY's ring breathing ( $1014\text{ cm}^{-1}$ ) and C=C stretching (deprotonated N) ( $1586\text{ cm}^{-1}$ ), and ATP's C–H bending + C–N stretching ( $1143\text{ cm}^{-1}$ ) and C–H bending ( $1186\text{ cm}^{-1}$ ) are assigned positive LV 2 scores. This signifies that the cumulative effect of peak intensity and/or peak position variances from these vibrational modes contribute to the classification of a breath profile as COVID-positive. On the other hand, MBA's C–S stretching ( $521\text{ cm}^{-1}$ ), MPY's C–H + N–H bending ( $1224\text{ cm}^{-1}$ ) and C=C stretching (protonated N), and ATP's N=N + C–N stretching ( $1393\text{ cm}^{-1}$ ) and N=N stretching + C–H bending ( $1441\text{ cm}^{-1}$ ) are assigned negative LV 2 scores and therefore are crucial in classifying COVID-negative breath profiles. This thus affirms that the amalgamation of multiple receptor spectral changes in our SERS superprofiles are important in assigning the COVID-positive or COVID-negative class. Furthermore, it proves that our model is built upon valid spectra variances arising from chemical interactions between receptor–BVOC and the change in BVOC concentrations and not spectral noise.

To emphasize the importance of the multireceptor SERS superprofile, we demonstrate the distinct sensitivity improvement from 80 to 96.2% when comparing a single SERS receptor with our SERS superprofile sensor (Figure 4E, Table S4, Supporting Information 3). An increase in the number of correctly classified COVID-positive breath profiles can be observed as the number of receptors increases from one to three. This increase exemplifies that each receptor imbues enhanced distinguishing capabilities to our SERS sensor by increasing the total number of distinct features between the breath profiles of COVID-positive and COVID-negative individuals. Such an approach is critical for complex sample matrices to allow our SERS sensor to record a more complete description of the differences in breath profiles. Notably, a high specificity can be achieved even with a single receptor as it is comparatively easier to distinguish a sensor that is exposed to breath, than accurately identifying a COVID-positive breath profile.

**Detailed Model Analysis in Relation to Clinical Test Results.** Through rigorous analysis of our clinical trial results, we highlight the key strengths of our SERS sensor based on its performance given a specific use case. The overall sensitivity of 96.2% (95% CI: 91.8–100%) and specificity of 99.9% (95% CI: 99.7–100%) can be derived by constructing a confusion matrix using the averaged classification outcomes across 50 model iterations (Figure 5A). Both the positive and negative predictive values (PPV and NPV) are >99%, indicating high accuracy of our PLSDA model in predicting the presence of COVID-19 at the disease prevalence of our clinical studies.<sup>34</sup> When considering the model sensitivity in relation to displayed COVID-19 symptoms, we note that our model shows high sensitivities of 97.7% and 93.6% for both symptomatic and asymptomatic individuals, respectively (Figure 5B). The slightly lower sensitivity when identifying asymptomatic COVID-positive individuals could be due to the limited sample size of 31 participants. To enhance the ability of our sensor in picking up asymptomatic COVID-positive individuals, it is essential to collect more data so as to elucidate spectral features, which are important for their classification. In addition, out of 70 participants with reported comorbidities including asthma and thyroid dysfunctions (4 COVID-positive, 66 COVID-negative), all 70 participants are accurately classified in their respective COVID-19 infection status (Figure S15). This indicates that the presence of pre-existing medical conditions does not affect the prediction outcome of our SERS breathalyzer.

Importantly, we demonstrate good representation of individuals at various stages of COVID-19 infection in our clinical trial with PCR cycle threshold (Ct) values ranging from <15 to >40 (Figure 5Ci). The PCR Ct value indicates the relative viral load in an infected individual, whereby a low Ct value is equivalent to a high viral load. Notably, the high sensitivity of our SERS sensor across a large range of Ct values indicates that there are distinct BVOC differences for all COVID-positive individuals regardless of the viral load in their bodies (Figure 5Cii). This is crucial in ensuring our breathalyzer's effectiveness in picking up infected individuals across all stages of infection, as these individuals may still be potentially infectious.<sup>35–37</sup>

In addition, we ascertain that other potential confounding factors such as age, gender, smoking habits, and time since the last meal do not significantly influence our classification, by employing the *t* test and  $\chi^2$  test (Figure 5D–F). Given a mean age of  $41 \pm 14$  years old for COVID-positive participants and  $43 \pm 13$  years old for COVID-negative participants, age did not

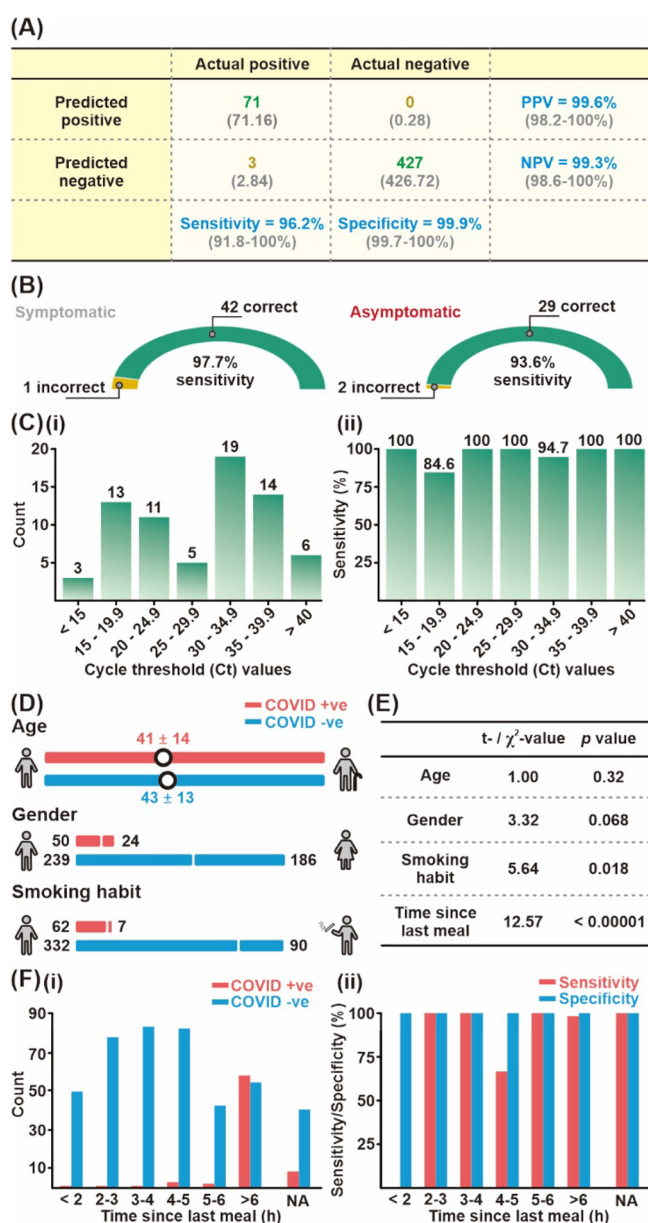


**Figure 5.** Detailed analysis of clinical trial results. (A) Confusion matrix of the averaged classification outcomes across 50 model iterations. Values in green and brown indicate correct and incorrect classification outcomes, respectively. Actual values before rounding off are given in gray brackets. The sensitivity, specificity, positive, and negative prediction values are in blue, with their corresponding 95% confidence intervals in gray brackets directly below. (B) Scheme depicting the sensitivity of our sensor in the classification of symptomatic and asymptomatic COVID-positive individuals. (C) Histogram depicting (i) the number of COVID-positive participants based on their respective cycle threshold (Ct) values determined by a PCR test and (ii) the model sensitivity at each Ct range. (D) Scheme describing participant demographics such as their mean age, gender, and smoking habits. (E) Summary table describing the statistical test results of potential confounding factors such as participants' age, gender, smoking habits, and time since the last meal using either the  $t$  test or  $\chi^2$  test, with their corresponding  $p$ -value. (F) Analysis of time since the last meal as a potential confounding factor based on (i) distribution of time since last meal of all participants (a small number of participants were unable to recall this information (denoted as NA) and (ii) the model sensitivity and specificity at each time range.

significantly influence our classification at the 95% confidence level ( $t = 1.00$ ,  $p = 0.32$ ). Similarly, the gender distribution of 50 males and 24 females across COVID-positive participants and 239 males and 186 females across COVID-negative participants did not affect our classification ( $\chi^2 = 3.32$ ,  $p = 0.068$ ). When investigating the effect of smoking habits, since only 6 COVID-positive and 90 COVID-negative participants smoke, we set a higher critical value of  $p = 0.01$ . At a 99% confidence level, the participants' smoking habits ( $\chi^2 = 5.64$ ,  $p = 0.018$ ) did not impact our classifications. However, a larger sample size is likely necessary in order to arrive at a more statistically robust conclusion for this factor. In terms of the time elapsed since the participants' last meal, there is significant imbalance as most COVID-positive participants (58 out of 66) did not consume any food for >6 h prior to the breathalyzer test (Figure SFi). This resulted in a significant difference between the average time since the last meal ( $t = 12.57$ ,  $p < 0.00001$ ) for COVID-positive and COVID-negative participants. This difference stems from an inherent limitation in operational protocol, as breath samples were typically collected from COVID-positive individuals by nurses before their breakfast at a specified timing. In contrast, breath samples from COVID-negative individuals were collected after disembarking from a flight, which had meals provided, with no restrictions as to when they are allowed to consume any food. Nonetheless, we note that even with such an imbalance, the high classification specificity of 99.9% is a clear indicator that the differences between COVID-positive and COVID-negative breath samples were much more pronounced compared to any differences in breath composition resulting from food consumption (Figure SFii).

## CONCLUSION

In conclusion, we showcase our design of a SERS-based breathalyzer for rapid, noninvasive screening of individuals for COVID-19, achieving a sensitivity of 96.2% and specificity of 99.9%. Through the strategic use of multiple molecular receptors to capture and interact with various BVOCs in exhaled breath, we generate highly informative SERS super-profiles that harness each receptor's distinguishing power. Fundamentally, we establish good qualitative agreement between our observed SERS spectral variances with those induced by pure VOC vapors of several potential COVID-19 biomarkers. The in-depth understanding of these spectral differences allows us to construct a robust PLSDA model which attains a false negative rate superior to commercially available antigen rapid tests and comparable to that of PCR tests. In addition, the classification accuracy is independent of whether the individual displays COVID-19-related symptoms and other confounding factors such as age, gender, and smoking habits before breath collection. Most importantly, our test is simple, easy to administer, and requires only 5 min from sample collection to output of results for rapid turnover. As the world adjusts to a new normal, government strategies are shifting toward scaling up of COVID-19 testing, contact tracing, and vaccination. In this aspect, our breathalyzer can play a significant role in fulfilling this goal by supporting mass screening capabilities even at locations with high human traffic. Breath collection and measurements can be performed in parallel, which overcomes the current bottleneck in conventional GC-MS methods for breath analysis, making it suitable for testing in diverse settings and locations like schools, airports, and events like weddings, religious events, and conferences. Moreover, our findings from this work lay the foundation for next-generation

breath-based detection of other respiratory and/or non-respiratory related diseases using SERS.

## MATERIALS AND METHODS

**Chemicals.** Silver nitrate, 1,5-pentanediol (PD), poly(vinylpyrrolidone) (PVP;  $M_w \sim 55,000$ ), 4-mercaptopyridine (MPY), 4-mercaptobenzoic acid (MBA), 4-aminothiophenol (ATP), ethanal, heptanal, and octanal were purchased from Sigma-Aldrich. Copper(II) chloride was purchased from Alfa Aesar. Ethanol (ACS, ISO, Reag. Ph Eur) was obtained from Merck. Methanol ( $\geq 99.8\%$ , Reag. Ph Eur, gradient grade for HPLC) was obtained from VWR Chemicals. Milli-Q water ( $>18.0\text{ M}\Omega\text{ cm}$ ) was purified with a Sartorius Arium 611 UV ultrapure water system. All reagents were used without further purification.

**Synthesis and Purification of Silver Nanocubes.** Ag nanocubes were synthesized via the polyol method described in literature.<sup>38</sup> Briefly, 0.50 g of silver nitrate and 0.86  $\mu\text{g}$  of copper(II) chloride were dissolved in PD in a scintillation vial. Separately, 0.25 g of PVP was dissolved in PD. Using a temperature-controlled silicone oil bath, 20 mL of PD was heated for 10 min. The two precursor solutions were then injected into the hot reaction flask at different rates: 500  $\mu\text{L}$  of silver nitrate solution every minute and 250  $\mu\text{L}$  of PVP solution every 30 s. This addition was stopped once the solution turned ochre. The Ag nanocubes were purified via several rounds of centrifugation and subsequently stored in ethanol. Scanning electron microscopic (SEM) imaging was carried out using JEOL-JSM-7600F electron microscope at an accelerating voltage of 5 kV.

**Thiophenol Functionalization of Ag Nanocubes.** Functionalization of Ag nanocube surfaces was performed through individual ligand exchange reactions. A 50  $\mu\text{L}$  aliquot of 10 mM thiophenol solution (MPY, MBA, ATP) was separately added to 1 mL of Ag nanocubes, and the mixture was allowed to stir overnight. The functionalized Ag nanocubes were then purified via centrifugation and dispersed in 1 mL ethanol.<sup>39</sup>

**Sensor Chip and Breathalyzer Fabrication.** An automated liquid dispensing system (Y&D 7300N Smart Robot; Y&D Technology Co. Ltd.) was used to dispense the functionalized Ag nanocubes. The functionalized Ag nanocubes were first dispersed in aqueous solutions, carefully loaded into the dispensing system, and then precisely dispensed onto an aluminum plate. The dispensed Ag nanocubes were then allowed to dry under controlled conditions (24 °C with relative humidity of 40%). SERS signals of the dried droplets were measured to ensure sensor chip signal reproducibility and consistency before they were individually assembled into a breathalyzer. The assembled breathalyzer and an accompanying cap were vacuum-sealed prior to its usage during clinical trials.

**Breath Sample Collection.** Participants aged between 18 and 99 were recruited at multiple study sites for clinical trials, including the National Center for Infectious Diseases and Changi International Airport in Singapore. All recruitment protocols were covered under NTU's IRB-2020-12-012 and IRB-2021-03-046. Study participants were adequately briefed regarding the research goals and aims, and their consent was sought prior to sample collection (Figure S1). All breathalyzers were deidentified from the study participants with the use of specialized subject identification numbers. During sample collection, a sealed vacuum package containing the breathalyzer was handed to the participant. The participant was directed to blow gently and continuously into the breathalyzer mouthpiece for 10 s before affixing the safety cap. The breathalyzer was then disinfected with 70% ethanol before SERS measurement. Each breathalyzer is fitted with medical grade HEPA filter at the outlet to isolate any pathogens present within the breath chamber and prevent escape into the external environment. Each participant exhaled into a breathalyzer that is assigned to them.

**SERS Measurement of Breath Samples.** SERS measurements were conducted using the portable Metrohm Raman spectrometer (Mira DS) with an excitation wavelength of 785 nm, laser power of 50 mW and an acquisition time of 0.05 s. Each SERS spectrum is the average of 5 raster scans (2.5 mm raster scan size), to collect SERS spectra over a large interrogation area. The spectral window of 400–

1800  $\text{cm}^{-1}$  was used for data analyses. Spectral preprocessing includes baseline correction using the adaptive iteratively reweighted penalized least-squares (airPLS) algorithm and min–max normalization.<sup>40</sup> The processed SERS spectra from all three receptors were then concatenated into a SERS superprofile representing the breath profile of a participant. A total of 501 superprofiles were collected—1 from each participant.

**Model Building.** The partial least-squares discriminant analysis (PLSDA) models were constructed using the Python-based scikit-learn package.<sup>41</sup> In one iteration, data were first split into a 80% train and 20% test set using random state = 1. The train set was optimized and cross-validated using a  $k$ -fold cross-validation algorithm, with  $k = 10$ . Root-mean-squared errors resulting from the train set classification and averaged cross-validation classifications were derived and used to determine the number of latent variables selected for a PLSDA model. The test set was then used to assess the outcome of our classification model through calculating its sensitivity and specificity. This process was then repeated for an additional 49 iterations using random states 2–50 to derive the averaged sensitivity and specificity of our SERS sensor.

**SERS Measurements of Pure Analyte Vapor.** The SERS sensor is incubated separately with 200  $\mu\text{L}$  of a target analyte at 35 °C in an enclosed 20 mL vial. SERS detection was performed after 6 h of incubation using the same spectrometer system, measurement parameters and data preprocessing. Equilibrium vapor concentrations are calculated in Supporting Information 2. For detection at low VOC concentrations, a vapor generator (Vertical Owlstone Vapor Generator, Owlstone Medical) is used to supply a constant, controlled VOC flow at ppb levels.

**Participant Statistics.** Participant statistics for categorical variables such as age and gender were presented as number (%). Continuous variables such as intensity ratios were presented as mean  $\pm$  standard deviation. The statistical significance of each variable between blanks and COVID-positive, blanks and COVID-negative, and COVID-positive and COVID-negative were assessed with the Mann–Whitney rank sum test. All tests were two-tailed with  $p < 0.05$  as the significance threshold. Calculations were performed using the OriginPro 9.0 software. The statistical significance of each confounding factor on the classification was assessed using either a  $t$  test (for continuous variable) or a  $\chi^2$  test (categorical variable). The choice of statistical test depends on several parameters including the variable type (categorical/continuous) and distributions (normal/non-normal).

**Density Functional Theory (DFT) Simulations.** The calculations on the interaction of the Ag surface with various target analyte molecules were carried out using the unrestricted B3LYP exchange–correlation functional, as implemented in the Gaussian 09 computational chemistry package. The 6-31G(d,p) basis set was used for all atoms except Ag, for which the LANL2DZ basis set was employed. The Ag surface was modeled using a reported triangle consisting of 6 Ag atoms.<sup>42</sup> After geometry optimization of the triangular Ag cluster, each target analyte molecule was then placed near the Ag cluster ( $<2\text{ \AA}$ ) and the entire system was reoptimized before obtaining the simulated spectra.

**Characterization.** Scanning electron microscope (SEM) imaging was performed using JEOL-JSM-7600F microscope. UV–vis spectra were measured using SHIMADZU UV-3600 UV–vis–NIR spectrophotometer.

## ASSOCIATED CONTENT

### Supporting Information

The Supporting Information is available free of charge at <https://pubs.acs.org/doi/10.1021/acsnano.1c09371>.

Participant recruitment workflow, Ag nanocube SEM and UV–vis characterization, full peak assignments, analytical enhancement factor calculations, sensor chip reproducibility and stability, PCA score plots of VOCs at different concentrations and different breath incubation times, VOC vapor concentration calculations, additional peak

analysis for MPY, ATP, and MBA, DFT calculations for MBA, individual PLSDA sensitivity and specificity metrics, sample sensitivity and specificity calculations (PDF)

## AUTHOR INFORMATION

### Corresponding Author

**Xing Yi Ling** – Division of Chemistry and Biological Chemistry, School of Physical and Mathematical Sciences, Nanyang Technological University, Singapore 637371, Singapore; [orcid.org/0000-0001-5495-6428](https://orcid.org/0000-0001-5495-6428); Email: [xyling@ntu.edu.sg](mailto:xyling@ntu.edu.sg)

### Authors

**Shi Xuan Leong** – Division of Chemistry and Biological Chemistry, School of Physical and Mathematical Sciences, Nanyang Technological University, Singapore 637371, Singapore

**Yong Xiang Leong** – Division of Chemistry and Biological Chemistry, School of Physical and Mathematical Sciences, Nanyang Technological University, Singapore 637371, Singapore

**Emily Xi Tan** – Division of Chemistry and Biological Chemistry, School of Physical and Mathematical Sciences, Nanyang Technological University, Singapore 637371, Singapore

**Howard Yi Fan Sim** – Division of Chemistry and Biological Chemistry, School of Physical and Mathematical Sciences, Nanyang Technological University, Singapore 637371, Singapore

**Charlynn Sher Lin Koh** – Division of Chemistry and Biological Chemistry, School of Physical and Mathematical Sciences, Nanyang Technological University, Singapore 637371, Singapore

**Yih Hong Lee** – Division of Chemistry and Biological Chemistry, School of Physical and Mathematical Sciences, Nanyang Technological University, Singapore 637371, Singapore

**Carice Chong** – Division of Chemistry and Biological Chemistry, School of Physical and Mathematical Sciences, Nanyang Technological University, Singapore 637371, Singapore

**Li Shiuan Ng** – Division of Chemistry and Biological Chemistry, School of Physical and Mathematical Sciences, Nanyang Technological University, Singapore 637371, Singapore

**Jaslyn Ru Ting Chen** – Division of Chemistry and Biological Chemistry, School of Physical and Mathematical Sciences, Nanyang Technological University, Singapore 637371, Singapore

**Desmond Wei Cheng Pang** – Division of Chemistry and Biological Chemistry, School of Physical and Mathematical Sciences, Nanyang Technological University, Singapore 637371, Singapore

**Lam Bang Thanh Nguyen** – Division of Chemistry and Biological Chemistry, School of Physical and Mathematical Sciences, Nanyang Technological University, Singapore 637371, Singapore

**Siew Kheng Boong** – Division of Chemistry and Biological Chemistry, School of Physical and Mathematical Sciences, Nanyang Technological University, Singapore 637371, Singapore

**Xuemei Han** – Division of Chemistry and Biological Chemistry, School of Physical and Mathematical Sciences, Nanyang Technological University, Singapore 637371, Singapore

**Ya-Chuan Kao** – Division of Chemistry and Biological Chemistry, School of Physical and Mathematical Sciences, Nanyang Technological University, Singapore 637371, Singapore

**Yi Heng Chua** – Division of Chemistry and Biological Chemistry, School of Physical and Mathematical Sciences, Nanyang Technological University, Singapore 637371, Singapore

**Gia Chuong Phan-Quang** – Division of Chemistry and Biological Chemistry, School of Physical and Mathematical Sciences, Nanyang Technological University, Singapore 637371, Singapore; Silver Factory Technology Pte. Ltd., Singapore 169203, Singapore

**In Yee Phang** – Silver Factory Technology Pte. Ltd., Singapore 169203, Singapore

**Hiang Kwee Lee** – Division of Chemistry and Biological Chemistry, School of Physical and Mathematical Sciences, Nanyang Technological University, Singapore 637371, Singapore; [orcid.org/0000-0003-0823-4111](https://orcid.org/0000-0003-0823-4111)

**Mohammad Yazid Abdad** – Infectious Diseases Research Laboratory, National Centre for Infectious Diseases, Singapore 308442, Singapore; Centre for Tropical Medicine and Global Health, Nuffield Department of Medicine, University of Oxford, Oxford OX3 7LG, U.K.; Faculty of Tropical Medicine, Mahidol University, Bangkok 10400, Thailand

**Nguan Soon Tan** – Lee Kong Chian School of Medicine, Nanyang Technological University, Singapore 308232, Singapore; School of Biological Sciences, Nanyang Technological University, Singapore 637551, Singapore

Complete contact information is available at:

<https://pubs.acs.org/10.1021/acsnano.1c09371>

### Author Contributions

The manuscript was written through contributions of all authors.

### Author Contributions

<sup>†</sup>S.X.L. and Y.X.L. contributed equally.

### Notes

The authors declare no competing financial interest.

## ACKNOWLEDGMENTS

This research is supported by National Medical Research Council, Singapore under COVID-19 Research Fund (MOH-COVID19RF-0007 and MOH-COVID19RF-0012), A\*STAR Singapore, AME Individual Research Grant (A20E5c0082) and Max Planck Institute-Nanyang Technological University Joint Lab. S.X.L. and L.B.T.N. acknowledge Nanyang Presidential scholarship support from Nanyang Technological University, Singapore. We thank Singapore Ministry of Health, Ministry of Transport, the National Center for Infectious Diseases (NCID), Singapore, Certis Cisco, Singapore, and Changi Airport Group, Singapore, for their support in arranging access to breath samples, in particular, Dr. Shawn Vasoo, Prof. Leo Yee Sin, Prof. Raymond Lin, Siti Nurdiana Abas, Nurhidayah Mohamed Yazid, Ong Jin Ting, Ivana Stevani, K. Renganathan, Amanda Tan, and Benjamin Goy from NCID, Lian Kay Wee and Sim Pei Wen from Changi Airport Group, Seah Hock Chye, Goh Ming Xuan, Joy Kwan, and Patrick Teo from Certis Cisco, as well as the student volunteers from Nanyang Technological University, Singapore, for their help in recruiting participants.

## REFERENCES

- (1) Chen, H.; Qi, X.; Ma, J.; Zhang, C.; Feng, H.; Yao, M. Breath-Borne VOC Biomarkers for COVID-19. *medRxiv* **2020**, DOI: 10.1101/2020.06.21.20136523.
- (2) Grassin-Delyle, S.; Roquencourt, C.; Moine, P.; Saffroy, G.; Carn, S.; Heming, N.; Fleuriot, J.; Salvator, H.; Naline, E.; Couderc, L.-J.; Devillier, P.; Thévenot, E. A.; Annane, D. Metabolomics of Exhaled Breath in Critically Ill COVID-19 Patients: A Pilot Study. *EBioMedicine* **2021**, 63, 103154.
- (3) Ruszkiewicz, D. M.; Sanders, D.; O'Brien, R.; Hempel, F.; Reed, M. J.; Riepe, A. C.; Bailie, K.; Brodrick, E.; Darnley, K.; Ellerkmann, R.; Mueller, O.; Skarysz, A.; Truss, M.; Wortelmann, T.; Yordanov, S.; Thomas, C. L. P.; Schaaf, B.; Eddleston, M. Diagnosis of COVID-19 by Analysis of Breath with Gas Chromatography-Ion Mobility Spectrometry - A Feasibility Study. *EClinicalMedicine* **2020**, 29, 100609.
- (4) Gupta, A.; Madhavan, M. V.; Sehgal, K.; Nair, N.; Mahajan, S.; Sehrawat, T. S.; Bikdeli, B.; Ahluwalia, N.; Ausiello, J. C.; Wan, E. Y.; Freedberg, D. E.; Kirtane, A. J.; Parikh, S. A.; Maurer, M. S.; Nordvig, A. S.; Accili, D.; Bathon, J. M.; Mohan, S.; Bauer, K. A.; Leon, M. B.; Krumholz, H. M.; Uriel, N.; Mehra, M. R.; Elkind, M. S. V.; Stone, G. W.; Schwartz, A.; Ho, D. D.; Bilezikian, J. P.; Landry, D. W. Extrapulmonary Manifestations of COVID-19. *Nat. Med.* **2020**, 26, 1017–1032.
- (5) Cao, W.; Duan, Y. Current Status of Methods and Techniques for Breath Analysis. *Crit. Rev. Anal. Chem.* **2007**, 37, 3–13.
- (6) Kim, K. H.; Jahan, S. A.; Kabir, E. A Review of Breath Analysis for Diagnosis of Human Health. *TrAC, Trends Anal. Chem.* **2012**, 33, 1–8.
- (7) Lawal, O.; Ahmed, W. M.; Nijssen, T. M. E.; Goodacre, R.; Fowler, S. J. Exhaled Breath Analysis: A Review of 'Breath-Taking' Methods for Off-Line Analysis. *Metabolomics* **2017**, 13, 110.
- (8) Lee, H. K.; Lee, Y. H.; Koh, C. S. L.; Phan-Quang, G. C.; Han, X.; Lay, C. L.; Sim, H. Y. F.; Kao, Y.-C.; An, Q.; Ling, X. Y. Designing Surface-Enhanced Raman Scattering (SERS) Platforms Beyond Hotspot Engineering: Emerging Opportunities in Analyte Manipulations and Hybrid Materials. *Chem. Soc. Rev.* **2019**, 48, 731–756.
- (9) Leong, Y. X.; Lee, Y. H.; Koh, C. S. L.; Phan-Quang, G. C.; Han, X.; Phang, I. Y.; Ling, X. Y. Surface-Enhanced Raman Scattering (SERS) Taster: A Machine-Learning-Driven Multireceptor Platform for Multiplex Profiling of Wine Flavors. *Nano Lett.* **2021**, 21, 2642–2649.
- (10) Koh, C. S. L.; Lee, H. K.; Han, X.; Sim, H. Y. F.; Ling, X. Y. Plasmonic Nose: Integrating the MOF-Enabled Molecular Preconcentration Effect with a Plasmonic Array for Recognition of Molecular-Level Volatile Organic Compounds. *Chem. Commun.* **2018**, 54, 2546–2549.
- (11) Sethi, S.; Nanda, R.; Chakraborty, T. Clinical Application of Volatile Organic Compound Analysis for Detecting Infectious Diseases. *Clin. Microbiol. Rev.* **2013**, 26, 462–75.
- (12) Capocefalo, A.; Mammucari, D.; Brasili, F.; Fasolato, C.; Bordi, F.; Postorino, P.; Domenici, F. Exploring the Potentiality of a SERS-Active pH Nano-Biosensor. *Front. Chem.* **2019**, 7, 413.
- (13) Wang, Y.; Ji, W.; Sui, H.; Kitahama, Y.; Ruan, W.; Ozaki, Y.; Zhao, B. Exploring the Effect of Intermolecular H-Bonding: A Study on Charge-Transfer Contribution to Surface-Enhanced Raman Scattering of P-Mercaptobenzoic Acid. *J. Phys. Chem. C* **2014**, 118, 10191–10197.
- (14) Guerrini, L.; Rodriguez-Loureiro, I.; Correa-Duarte, M. A.; Lee, Y. H.; Ling, X. Y.; García de Abajo, F. J.; Alvarez-Puebla, R. A. Chemical Speciation of Heavy Metals by Surface-Enhanced Raman Scattering Spectroscopy: Identification and Quantification of Inorganic- and Methyl-Mercury in Water. *Nanoscale* **2014**, 6, 8368–8375.
- (15) Bi, L.; Wang, Y.; Yang, Y.; Li, Y.; Mo, S.; Zheng, Q.; Chen, L. Highly Sensitive and Reproducible SERS Sensor for Biological pH Detection Based on a Uniform Gold Nanorod Array Platform. *ACS Appl. Mater. Interfaces* **2018**, 10, 15381–15387.
- (16) Wang, Y.; Yu, Z.; Ji, W.; Tanaka, Y.; Sui, H.; Zhao, B.; Ozaki, Y. Enantioselective Discrimination of Alcohols by Hydrogen Bonding: A SERS Study. *Angew. Chem., Int. Ed.* **2014**, 53, 13866–13870.
- (17) Xu, P.; Kang, L.; Mack, N. H.; Schanze, K. S.; Han, X.; Wang, H.-L. Mechanistic Understanding of Surface Plasmon Assisted Catalysis on a Single Particle: Cyclic Redox of 4-Aminothiophenol. *Sci. Rep.* **2013**, 3, 2997.
- (18) Huang, Y.-F.; Zhu, H.-P.; Liu, G.-K.; Wu, D.-Y.; Ren, B.; Tian, Z.-Q. When the Signal Is Not from the Original Molecule to Be Detected: Chemical Transformation of Para-Aminothiophenol on Ag During the SERS Measurement. *J. Am. Chem. Soc.* **2010**, 132, 9244–9246.
- (19) Liu, Y.; Yang, D.; Zhao, Y.; Yang, Y.; Wu, S.; Wang, J.; Xia, L.; Song, P. Solvent-Controlled Plasmon-Assisted Surface Catalysis Reaction of 4-Aminothiophenol Dimerizing to p,p'-Dimercaptoazobenzene on Ag Nanoparticles. *Heliyon* **2019**, 5, e01545.
- (20) Wu, D.-Y.; Zhao, L.-B.; Liu, X.-M.; Huang, R.; Huang, Y.-F.; Ren, B.; Tian, Z.-Q. Photon-Driven Charge Transfer and Photocatalysis of P-Aminothiophenol in Metal Nanogaps: A DFT Study of SERS. *Chem. Commun.* **2011**, 47, 2520–2522.
- (21) Barker, M.; Rayens, W. Partial Least Squares for Discrimination. *J. Chemom.* **2003**, 17, 166–173.
- (22) Brereton, R. G.; Lloyd, G. R. Partial Least Squares Discriminant Analysis: Taking the Magic Away. *J. Chemom.* **2014**, 28, 213–225.
- (23) Wold, S.; Sjöström, M.; Eriksson, L. PLS-Regression: A Basic Tool of Chemometrics. *Chemom. Intell. Lab. Syst.* **2001**, 58, 109–130.
- (24) Westerhuis, J. A.; Hoefsloot, H. C. J.; Smit, S.; Vis, D. J.; Smilde, A. K.; van Velzen, E. J. J.; van Duijnhoven, J. P. M.; van Dorsten, F. A. Assessment of PLS-DA Cross Validation. *Metabolomics* **2008**, 4, 81–89.
- (25) Xu, Q.-S.; Liang, Y.-Z. Monte Carlo Cross Validation. *Chem. Intell. Lab. Syst.* **2001**, 56, 1–11.
- (26) Fouzas, S. SARS-CoV-2 Rapid Antigen Detection Tests. *Lancet. Infect. Dis.* **2021**, 21, 1068–1069.
- (27) Wikramaratna, P.; Paton, R. S.; Ghafari, M.; Lourenço, J. Estimating False-Negative Detection Rate of SARS-CoV-2 by RT-PCR. *medRxiv* **2020**, DOI: 10.1101/2020.04.05.20053355v3.
- (28) Xie, X.; Zhong, Z.; Zhao, W.; Zheng, C.; Wang, F.; Liu, J. Chest Ct for Typical Coronavirus Disease 2019 (COVID-19) Pneumonia: Relationship to Negative RT-PCR Testing. *Radiology* **2020**, 296, E41–E45.
- (29) Chang, M. C.; Lee, W.; Hur, J.; Park, D. Chest Computed Tomography Findings in Asymptomatic Patients with COVID-19. *Respiration* **2020**, 99, 748–754.
- (30) Meng, H.; Xiong, R.; He, R.; Lin, W.; Hao, B.; Zhang, L.; Lu, Z.; Shen, X.; Fan, T.; Jiang, W.; Yang, W.; Li, T.; Chen, J.; Geng, Q. CT Imaging and Clinical Course of Asymptomatic Cases with COVID-19 Pneumonia at Admission in Wuhan, China. *J. Infect.* **2020**, 81, e33–e39.
- (31) Goodpaster, A. M.; Kennedy, M. A. Quantification and Statistical Significance Analysis of Group Separation in NMR-Based Metabonomics Studies. *Chemom. Intell. Lab. Syst.* **2011**, 109, 162–170.
- (32) Xia, J.; Sinelnikov, I. V.; Han, B.; Wishart, D. S. Metaboanalyst 3.0—Making Metabolomics More Meaningful. *Nucleic Acids Res.* **2015**, 43, W251–7.
- (33) Phillips, M.; Herrera, J.; Krishnan, S.; Zain, M.; Greenberg, J.; Cataneo, R. N. Variation in Volatile Organic Compounds in the Breath of Normal Humans. *J. Chromatogr. B Biomed. Sci. Appl.* **1999**, 729, 75–88.
- (34) Wong, H. B.; Lim, G. H. Measures of Diagnostic Accuracy: Sensitivity, Specificity, PPV and NPV. *Proc. Singapore Healthc.* **2011**, 20, 316–318.
- (35) Gandhi, M.; Yokoe, D. S.; Havlir, D. V. Asymptomatic Transmission, the Achilles' Heel of Current Strategies to Control COVID-19. *N. Engl. J. Med.* **2020**, 382, 2158–2160.
- (36) Tian, D.; Lin, Z.; Kriner, E. M.; Esneault, D. J.; Tran, J.; DeVoto, J. C.; Okami, N.; Greenberg, R. M.; Yanofsky, S.; Ratnayaka, S.; Tran, N.; Livaccari, M.; Lampp, M. L.; Wang, N.; Tim, S.; Norton, P.; Scott, J.; Hu, T. Y.; Garry, R.; Hamm, L.; Delafontaine, P.; Yin, X. M. Ct Values Do Not Predict Severe Acute Respiratory Syndrome Coronavirus 2 (SARS-CoV-2) Transmissibility in College Students. *J. Mol. Diagn.* **2021**, 23, 1078–1084.
- (37) Gao, Z.; Xu, Y.; Sun, C.; Wang, X.; Guo, Y.; Qiu, S.; Ma, K. A Systematic Review of Asymptomatic Infections with COVID-19. *J. Microbiol., Immunol. Infect.* **2021**, 54, 12–16.

- (38) Tao, A.; Sinsermsuksakul, P.; Yang, P. Polyhedral Silver Nanocrystals with Distinct Scattering Signatures. *Angew. Chem., Int. Ed.* **2006**, *45*, 4597–4601.
- (39) Sim, H. Y. F.; Lee, H. K.; Han, X.; Koh, C. S. L.; Phan-Quang, G. C.; Lay, C. L.; Kao, Y.-C.; Phang, I. Y.; Yeow, E. K. L.; Ling, X. Y. Concentrating Immiscible Molecules at Solid@MOF Interfacial Nanocavities to Drive an Inert Gas–Liquid Reaction at Ambient Conditions. *Angew. Chem., Int. Ed.* **2018**, *57*, 17058–17062.
- (40) Zhang, Z.-M.; Chen, S.; Liang, Y.-Z. Baseline Correction Using Adaptive Iteratively Reweighted Penalized Least Squares. *Analyst* **2010**, *135*, 1138–1146.
- (41) Pedregosa, F.; Varoquaux, G.; Gramfort, A.; Michel, V.; Thirion, B.; Grisel, O.; Blondel, M.; Prettenhofer, P.; Weiss, R.; Dubourg, V. Scikit-Learn: Machine Learning in Python. *J. Mac. Learn. Res.* **2011**, *12*, 2825–2830.
- (42) You, T.-t.; Yin, P.-g.; Jiang, L.; Lang, X.-f.; Guo, L.; Yang, S.-h. *In Situ* Identification of the Adsorption of 4,4'-Thiobisbenzenethiol on Silver Nanoparticles Surface: A Combined Investigation of Surface-Enhanced Raman Scattering and Density Functional Theory Study. *Phys. Chem. Chem. Phys.* **2012**, *14*, 6817–6825.